# The Use of Physical-informational Neural Networks in the Field of Electromagnetic Field Solving

Tong Ben<sup>1</sup>, Wenguang Ke<sup>1</sup>, Long Chen<sup>3\*</sup>, Libing Jing<sup>2</sup>, and Xin Qi<sup>1</sup>

<sup>1</sup>College of Electrical Engineering and New Energy, China Three Gorges University, Yichang 443002, Hubei Province, China <sup>2</sup>Hubei Provincial Research Center on Microgrid Engineering Technology (China Three Gorges University), Yichang 443002, Hubei Province, China

<sup>3</sup>Hubei Provincial Engineering Technology Research Center for Power Transmission Line, China Three Gorges University, Yichang, 443002, China

(Received 16 April 2025, Received in final form 10 June 2025, Accepted 10 June 2025)

The current underutilization of existing physics-informed neural networks (PINN) in the domain of electromagnetic fields necessitates a concerted effort to facilitate the gradual transition from finite element methods to PINN. The complexity of simulating electric fields across various media using PINN presents significant challenges, particularly when addressing multiple equations and media in the context of magnetic field analysis, where numerous magnetic field quantities must be resolved. This study employs PINN to achieve the solution of the electric field at a simple boundary, enabling the simulation of electric fields in diverse media by accounting for varying conductivity. Additionally, the research addresses the dynamics of electric field solutions in response to time-varying boundaries. Subsequently, multiple equations are encoded concurrently, and boundary conditions are established to facilitate the simultaneous prediction of multiple magnetic fields. Ultimately, the methodology addresses the resolution of vector magnetic fields in nonlinear materials across multiple media. The accuracy of the proposed approach is corroborated through a comparative analysis with the finite element method.

Keywords: PINN, electromagnetic fields, different conductivities, FEA

#### 1. Introduction

In order to achieve the most effective design of electromagnetic (EM) machines, it is crucial to perform numerous simulations of the problem, each involving minor modifications to the parameters. Established numerical techniques, such as the Finite Element Method (FEM) [1] and the Finite Difference Method (FDM) [2], are frequently employed. The time required for each computation remains constant, irrespective of the extent of the changes made. Conversely, Deep Learning (DL) models can be leveraged to capitalize on the commonalities among various designs, thereby enhancing computational efficiency [3], which renders them a compelling alternative.

The last decade has witnessed transformative progress

©The Korean Magnetics Society. All rights reserved. \*Corresponding author: Tel: +86-18522089362

e-mail: chenlong@ctgu.edu.cn

in diverse fields, particularly computer vision and natural language processing [4], largely fueled by deep learning and the application of deep neural networks (DNNs). Despite these remarkable achievements, the adoption of deep learning techniques in numerical computing remains limited. For example, in the realm of electromagnetic field (EMF) prediction, deep learning models that utilize dense regression convolutional neural networks (CNNs) [5-7] have been implemented and have shown encouraging results. These CNN-based architectures are designed to process two-dimensional input data, where geometric and excitation information is represented as a structured array of pixelated data points. However, this approach necessitates the integration of supplementary data and the maintenance of a fixed segment of the CNN framework. Additionally, the training process is resourceintensive, as it requires a substantial amount of data, leading to inefficiencies; excessive data may be allocated to the input phase, rendering the predictions nearly inconsequential. Consequently, there is a pressing need

for a deep learning methodology that either minimizes data requirements or operates effectively with limited data for the prediction of magnetic fields.

PINN represents a methodology that necessitates minimal data input [6-8]. This innovative deep learning approach integrates partial differential equations (PDEs), boundary conditions (BCs), and initial conditions within a neural network framework, utilizing automatic differentiation for implementation. The solution is subsequently optimized through the minimization of a loss function to effectively tackle the margin challenge, as outlined in previous studies [9-11]. As a method for solving PDEs, PINNs show considerable promise and are gaining recognition [12]. Recently, it has attracted considerable attention and has been the subject of extensive research across various domains, including computational fluid dynamics [13], power systems [14], biomedical engineering [15], and inverse problems in multiple fields [16-18]. Reports indicate that PINN demonstrates a robust capability to address nonlinear problems with high spatial and temporal resolution [19], and it does so without the necessity for time-stepping, in contrast to conventional scientific computing techniques [20].

While the application of PINN has been extensively explored in the context of partial differential equations related to fluid dynamics, heat transfer, and mechanical problems, there is a notable scarcity of studies addressing their use in electromagnetic analysis. This research seeks to address this deficiency by investigating the applicability of PINN in low-frequency electromagnetic scenarios, as well as assessing its feasibility and performance.

The application of two-dimensional magnetic proximity fields in electromagnetic devices and systems presents a compelling opportunity for resolution through PINN [8, 21, 22]. PINNs have garnered significant attention across various engineering disciplines due to their ability to effectively address real-world challenges by simultaneously modeling empirical data and adhering to fundamental physical principles. One of the key advantages of PINN is that their computational cost remains invariant regardless of the number of collocation points, which alleviates the traditional computational demands associated with highdimensional problem-solving [9, 23]. Furthermore, the PINN framework is well-suited for addressing inverse problems and parametric design issues by utilizing advanced stochastic optimization methods and parallel computing resources [21, 24].

However, the application of PINN to the resolution of magnetic fields in electromagnetic systems continues to encounter several challenges. Primarily, the complexity of electromagnetic device solutions complicates their encoding within the PINN framework. Furthermore, the computational domain in electromagnetism often encompasses various media [25], which complicates the computational process. Additionally, traditional methodologies for addressing problems that utilize the vector potential of the magnetic field require the calculation of spatial derivatives of the intrinsic parameters [26]. These derivatives, particularly at internal boundaries, can be difficult to determine and may lead to instability during the training of the PINN. Moreover, in the case of nonlinear media where the parameterization is contingent upon the field, the necessity to repeatedly compute the spatial derivatives of the parameterization throughout the training cycle significantly hampers the training efficiency of the PINN.

To address the aforementioned challenges, it is suggested that the learning library of PINN, specifically deepxde [27], be utilized to analyze the electric field across various media and boundary conditions. Enhancements have been made to the PINN architecture designed for the resolution of two-dimensional static magnetic fields, aimed at increasing training efficiency and streamlining the code. Additionally, the proposed methodology seeks to concurrently ascertain both the magnetic intensity and the magnetic potential vector, thereby obviating the necessity for calculating spatial differential operators of the intrinsic parameters. The approach also includes the resolution of the distribution of multi-dielectric vector magnetic potentials in nonlinear materials. The accuracy of this methodology is corroborated through a comparative analysis with results obtained from the finite element method. The introduced PINN network is readily adaptable for addressing nonlinear problems that involve multiple interrelated physical fields.

In order to substantiate the efficacy of PINN as a feasible approach for electromagnetic applications, the problem framework incorporates a range of issues with varying levels of complexity, while considering aspects such as geometric configurations, material properties, and boundary conditions. Notably, the method exhibits a high degree of accuracy in its solutions. The reference data, utilized for comparison with the labeled data, is derived from a traditional finite element analysis solver.

## 2. Neural Network Modeling of Physical Information in Electromagnetic Fields

### 2.1. Traditional Physical-Informational Neural Networks

The conventional physical-informational neural network represents a framework wherein physical information is integrated with partial differential equations. However, this model is associated with several significant drawbacks, including its complexity and the cumbersome nature of its coding process. Additionally, a high degree of expertise is necessary to effectively encode the physical information required for problem-solving. Moreover, the inherent challenges in electromagnetism, characterized by a multitude of partial differential equations, often necessitate the simultaneous resolution of several such equations along with complex boundary conditions, thereby complicating the application of electromagnetism.

In the foundational setup, PINN integrates two learning strategies: an agent approximator and a partial differential equation learning network. The component of the loss function about PDE learning is articulated as a residual function, which aligns with a form of unsupervised learning paradigm. PINNs enable point-wise evaluation across the simulation domain, eliminating the need for mesh generation, they are regarded as "meshless" methodologies that leverage automatic differentiation (AD) for executing differentiation operations? the schematic diagram is shown in Fig. 1.

The principle of PINN can be outlined as below:

- 1) Construct  $NN\hat{u}(X;\theta)$  and adjustable coefficients (trainable parameters)  $\theta$ .
- 2) Use automatic differentiation (AD) to generate the necessary difference terms.
- 3) Define the training error component of the PDE  $(L_1)$ , the boundary conditions  $(L_2)$ , and the solution continuity of the interface  $(L_3)$ .

$$MSE = L_1 + L_2 + L_3 \tag{1}$$

4) Optimize the neural network by training it to determine the optimal parameters by minimizing the overall loss function  $(\theta')$ 

In practical applications, achieving a high level of accuracy necessitates the meticulous adjustment of all hyperparameters, such as the dimensions of the network, the learning rate, and the number of residual locations.

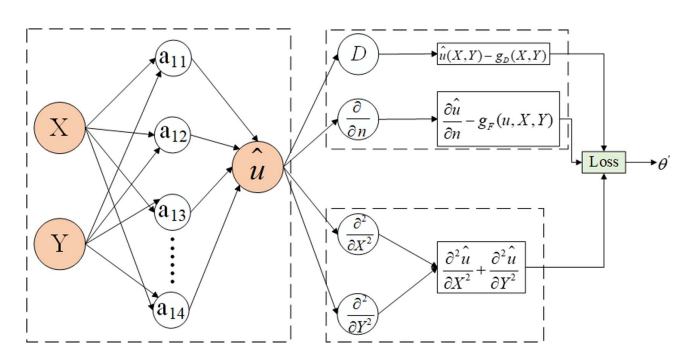


Fig. 1. (Color online) PINN solving schematic.

When establishing suitable network dimensions for partial differential equation problems, the smoothness characteristics of the analytical solution emerge as a pivotal determining factor.

This study involves the selection of a variety of problems characterized by varying degrees of complexity in order to determine the steady-state solutions for electrostatic and static magnetic scenarios, utilizing constant Dirichlet and Neumann boundary conditions.

### 2.2. Solving Partial Differential Equations for Electric and Magnetic Fields Using PINN

Many partial differential equations are involved in solving electric and magnetic fields, among which Laplace's equation is involved in solving the electric field, which is formulated as follows:

$$\nabla^2 u = \frac{\partial^2 u}{\partial X^2} + \frac{\partial^2 u}{\partial Y^2} + \frac{\partial^2 u}{\partial Z^2} = 0$$
 (2)

Where u is the voltage, X, Y and Z represent the X, Y and Z axes, and  $\nabla^2$  is the Laplace operator.

Since the two-dimensional equations are discussed in this paper, the Laplace equation can be simplified to the 2D Laplacian equation, which is given as follows:

$$\nabla^2 u = \frac{\partial^2 u}{\partial X^2} + \frac{\partial^2 u}{\partial Y^2} = 0 \tag{3}$$

Utilizing Laplace's equation, along with initial and boundary conditions, the solution to the electric field equation can be obtained by configuring the PINN code and establishing the Dirichlet and Neumann boundary conditions. This approach facilitates the derivation of the electric field distribution at various locations.

Whereas in the magnetic field solution process, which involves Maxwell's equations and ignores the electric displacement flux density, Ampere's law for stationary magnetic fields can be derived.:

$$\nabla \times H = J_i \tag{4}$$

Where  $J_i$  is the applied current density. In the context of static magnetization, the eddy current density is excluded. The magnetic field strength H is associated with the vector potential A by:

$$\mu_0 \mu_r H = B = \nabla \times A \tag{5}$$

Where  $\mu_0$  is the vacuum permeability,  $\mu_r$  is the relative permeability, B is the magnetic flux density, and A is the magnetic vector potential. For the two-dimensional case

utilizing the Cartesian coordinate framework, (4) and Eq. (5) extend to:

$$\left(\frac{\partial H_{y}}{\partial X} - \frac{\partial H_{x}}{\partial Y}\right) = J_{i} \tag{6}$$

$$\begin{cases}
\mu_0 \mu_r H_x = \frac{\partial A}{\partial Y} \\
\mu_0 \mu_r H_y = -\frac{\partial A}{\partial X}
\end{cases}$$
(7)

The subscripts signify the constituents in every direction. The magnetic field  $H_x$ ,  $H_y$  and vector potentials A in (6)-(7) are solved simultaneously by PINN. And the boundary conditions of  $H_x$ ,  $H_y$  and A are also required:

$$H_{\rm n}\big|_{\Gamma} = 0, \ A\big|_{\Gamma} = 0$$
 (8)

Above (6)-(8) are edge-valued problems to be solved.

#### 3. Electromagnetic Field Verification Case

#### 3.1. Solving simple boundary electric field equations

The basic two-dimensional Laplace equation for the electrostatic domain can be employed to characterize the stable solution of the electrostatic issue, tailored to accommodate Dirichlet and Neumann boundary conditions. The CAD drawing of the case is shown in Fig. 2. Examine the two-dimensional Laplace equation within a square region  $\Gamma$ :

$$-\nabla^2 u(X,Y) = 0, (X,Y) \in \Gamma$$
 (9)

For Case 1, the boundary specifications are outlined as follows:

$$u(0,Y) = 8V \tag{10}$$

$$u(2,Y) = 10V \tag{11}$$

For Case 2, the boundary specifications are outlined as follows?

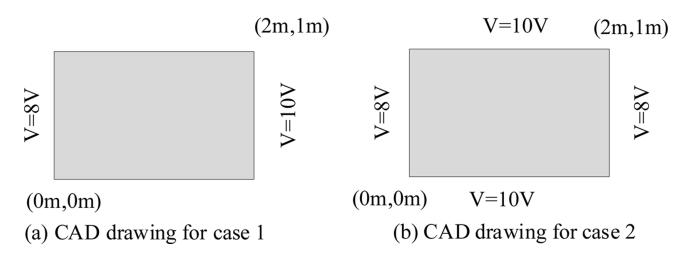


Fig. 2. Corresponding CAD drawings for electric field cases.

$$u(0,Y) = u(2,Y) = 8V$$
 (12)

$$u(X,0) = u(X,1) = 10V$$
 (13)

Two neural networks (NN) are independently trained to approximate the solution. The loss function, as delineated in Eq. (1), does not contain  $L_3$  because there is no interface condition in the problem, leading to the exclusion of an interface loss function. The implementation of two-dimensional Laplacian equations and boundary conditions, in conjunction with PINN coding, utilizes the deepxde library, which facilitates the efficient development of the code and significantly improves its versatility. The configuration of the electric field is addressed, and concurrently, it is analyzed using the finite element method. Subsequently, the discrepancies between the two solutions are assessed to validate their accuracy.

Due to the temporal variation of certain boundary conditions associated with the electric field in the present problem, it is essential to analyze the solution of the electric field equations within the three-dimensional framework defined by the X, Y, and T axes. In this context, the left boundary is established at 0V, while the right boundary is defined along the longitudinal axis of T, adhering to the relevant boundary conditions outlined in this study. Consequently, the boundary condition for voltage at the right boundary is set to be equal to T. The corresponding three-dimensional partial differential equation is formulated as follows:

$$\nabla^2 u = \frac{\partial^2 u}{\partial X^2} + \frac{\partial^2 u}{\partial Y^2} + \frac{\partial^2 u}{\partial T^2} = 0$$
 (14)

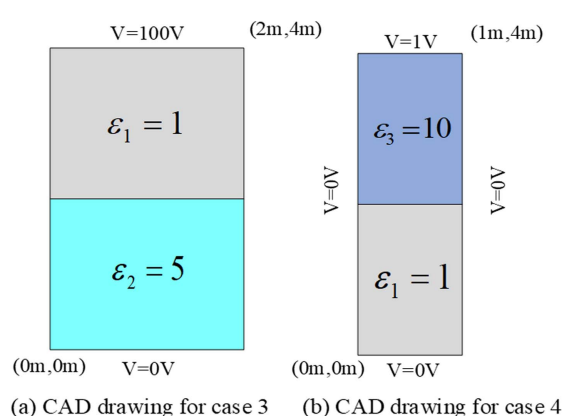
$$u(0,Y,T) = 0V \tag{15}$$

$$u(1,Y,T) = TV \tag{16}$$

#### 3.2. Multi-dielectric electric field solution

Given the diverse conductivities present in various media, it is essential to address distinct electric field scenarios, which requires the individual coding of conductivities for each medium in conjunction with their respective initial and boundary conditions. This approach is employed to model a basic parallel-plate capacitor, utilizing three boundaries corresponding to different media as a case study. The computer-aided design (CAD) representation of this case is illustrated in Fig. 3. This scenario can be conceptualized as two materials that share a common interface, governed by the following equations:

$$-\nabla \cdot \left(\varepsilon_{i} \cdot \nabla u\left(X,Y\right)\right) = 0, \left(X,Y\right) \in \Gamma_{i} \tag{17}$$



(a) CAD drawing for case 3 (b) CAD drawing for case 4

Fig. 3. (Color online) Corresponding CAD drawings for different dielectric electric field cases.

For Case 3, the boundary specifications are outlined as follows:

$$u(X,0) = 0V \tag{18}$$

$$u(X,4) = 100V$$
 (19)

For Case 4, the boundary specifications are outlined as follows:

$$u(X,0) = u(0,Y) = u(1,Y) = 0V$$
 (20)

$$u(X,1) = 1V \tag{21}$$

In the simulation of the electric field across various media, a singular neural network is employed to determine the solution, maintaining a consistent form of the partial differential equation while varying the magnetic permeabilities.

### 3.3. Simultaneous solution of multiple magnetic field quantities

The formulation of magnetic field dynamics inherently exhibits greater mathematical complexity compared to electric field descriptions, necessitating that Maxwell's equations be solved as a coupled system while simultaneously satisfying spatially and temporally varying initial-boundary value constraints. In this context, a straightforward magnetic field is examined as a case study by encoding several equations to be solved simultaneously. The subsequent quantities can be addressed concurrently.

In the initial phase of development, a neural network model is constructed to predict outcomes associated with the boundary value problem (BVP). For the network's input configuration, positional data from strategically selected collocation points within the computational domain are utilized, and the outputs of the neural network are  $H_x$ ,  $H_y$  and A. Then (6)-(8) are repeated into residual form:

$$\begin{cases} res_{I} = \left(\frac{\partial H_{y}}{\partial X} - \frac{\partial H_{x}}{\partial Y}\right) - J_{i} \\ res_{2} = \mu_{0}\mu_{r}H_{x} - \frac{\partial A}{\partial Y} \\ res_{3} = \mu_{0}\mu_{r}H_{y} + \frac{\partial A}{\partial X} \end{cases}$$
(22)

$$res_{\perp} = A|_{\Gamma}$$
,  $res_{\perp} = H_{n}|_{\Gamma}$ ,... (23)

The schematic diagram is shown in Fig. 4. Subsequently, the residuals are utilized to calculate the loss function. The location derivatives in equations (19), (20) are acquired through automatic differentiation (AD). AD utilizes the chain rule in conjunction with backpropagation to ascertain the derivatives of the neural network's

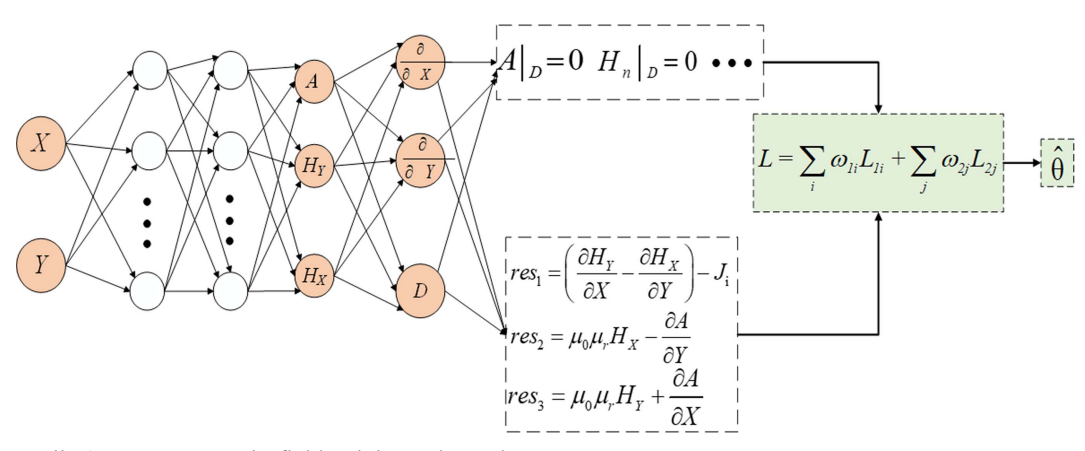


Fig. 4. (Color online) PINN magnetic field solving schematic.

outputs concerning its inputs, thus obtaining the position derivatives of  $H_x$ ,  $H_y$  and A. In contrast to the finite difference method, the AD algorithm excels in efficiency, and numerical stability, and exhibits superior compatibility with neural networks.

Subsequently, the loss associated with the neural network is evaluated. The overall loss is determined for the collocation points situated at both the internal and external boundaries of the domain. Derived from spatially distributed residuals, the total loss function undergoes optimization via gradient-based methods including adaptive moment estimation (Adam), stochastic gradient descent (SGD), and limited-memory BFGS (L-BFGS). This optimization procedure entails continuous refinement of neuronal weights and biases across all layers. As the loss converges to its minimum, the trained network's predictions satisfy the mathematical formulation presented in equations (6)-(8), thereby providing a numerical solution to the underlying PDE. Upon completion of the training phase, the field solution at any specified location (X, Y) can be derived through forward propagation of the neural network (prediction).

Silicon steel sheet, specifically of grade B30P105, is utilized as the medium in this study. The relative permeability of the material is established at 10,000, while the displacement current density is designated as 1A/mm². The corresponding CAD drawing is presented in Fig. 5. These parameters are encoded alongside various equations, and the pertinent boundary conditions are defined. Following this, the training process is conducted.

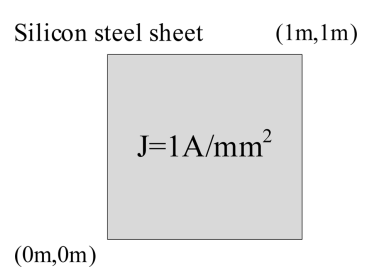


Fig. 5. CAD drawing of the magnetic field solution case.

#### 3.4. Vector magnetic potential solution for multidielectric magnetic fields of nonlinear materials

Since the magnetic permeability of nonlinear materials is nonlinear and varies at each point, solving for complex multi-materials becomes more complicated. The traditional solution method, generally the finite element method, is time-consuming and wasteful of computational resources. Therefore, this paper aims to find a method for solving the vectorial magnetic potential of nonlinear multi-dielectric materials by utilizing PINN. To ascertain the precision and viability of the PINN-derived solution, Epstein's square circle is used as a case study. Fig. 6 below depicts the physical figure of the Epstein square ring along with its 2D CAD drawing.

The system comprises three components: air, a silicon steel sheet, and a copper coil. A total of four sets of coils are employed, with one set conducting forward current and another set conducting reverse current. The silicon steel sheet, positioned centrally among the coils, is classified as B30P105 and delineates a square area, while

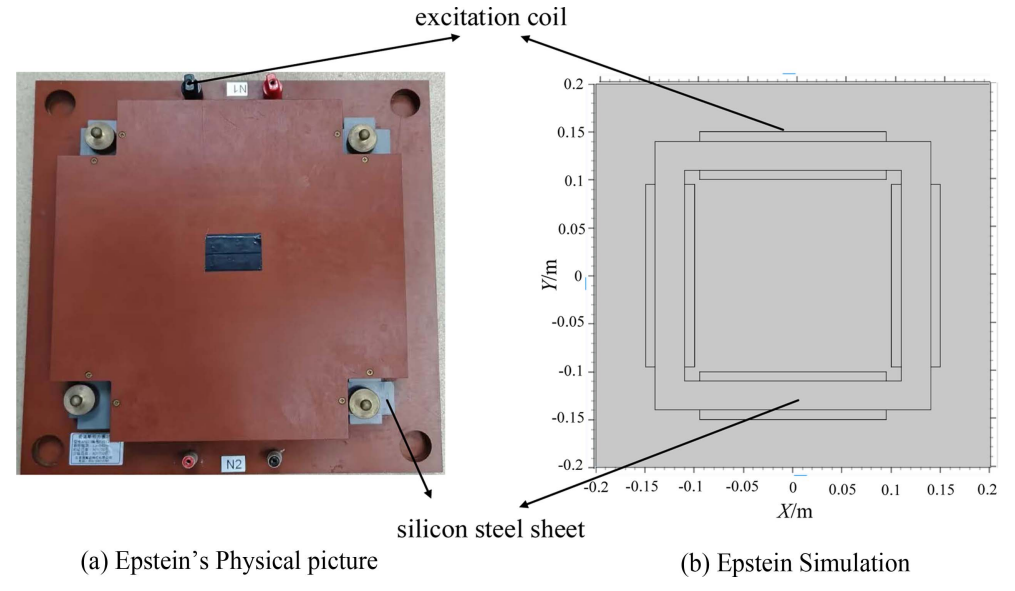


Fig. 6. (Color online) Epstein's Square Circle Physical and Simulation Diagrams.

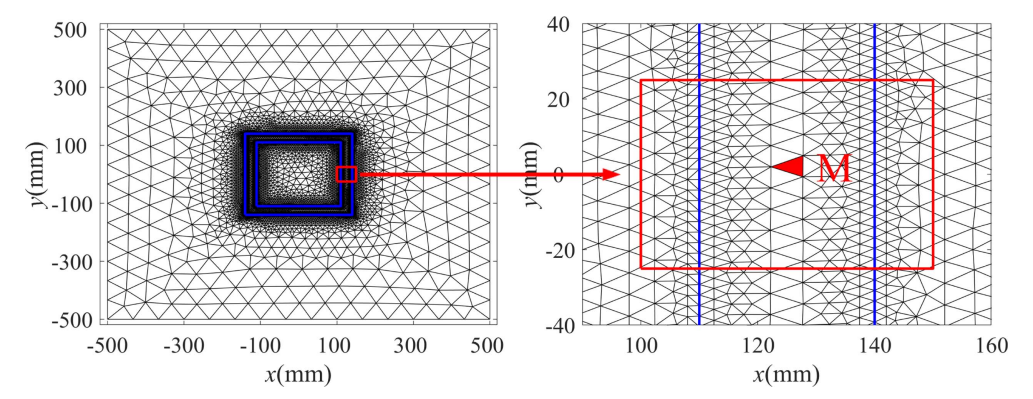


Fig. 7. (Color online) Finite element section of Epstein's square circle.

air envelops both the coils and the silicon steel sheet. As a nonlinear material characterized by fluctuating magnetic permeability at various internal points, the silicon steel sheet introduces a more complex problem. In the subsequent analysis, PINN will be applied to address the magnetic field associated with this configuration.

Meanwhile, the two-dimensional mesh dissection of Epstein's square circle is shown in Fig. 7. To prove the accuracy of the finite element model construction, the laboratory built a measurement platform, and the triangular mesh M in the middle region of the right column of Epstein's square circle was selected as the experimental measurement data for comparing with the calculation results of the finite element model.

The partial differential equation it satisfies is given by:

$$\nabla^2 A = -\mu J_{\tau} \tag{24}$$

Where  $\nabla^2$  is the Laplace operator, A is the vector magnetic potential,  $\mu$  is the magnetic permeability,  $J_z$  is the displacement current density perpendicular to the

direction of the paper, which is energized by the coil, and is given by:

$$J_{z} = \frac{NI_{\text{coil}}}{S} e_{\text{coil}}$$
 (25)

Where N is the number of coil turns,  $I_{\text{coil}}$  is the coil current, S is the coil area, and  $e_{\text{coil}}$  is the unit direction vector. Due to the magnetic insulation, the boundary condition is that the magnetic vector magnetic potential at the outer boundary is 0, and for the air region:

$$J_{z} = 0 \tag{26}$$

#### 4. Results and Discussion

### 4.1. Comparison of results for simple boundary electric field equations

As illustrated in Fig. 8(a) and Fig. 8(b), the double-boundary iteration progressively approaches its minimum value at approximately 17000 generations, resulting in a reduction of the loss function from 10<sup>2</sup> to 10<sup>-6</sup>. Con-

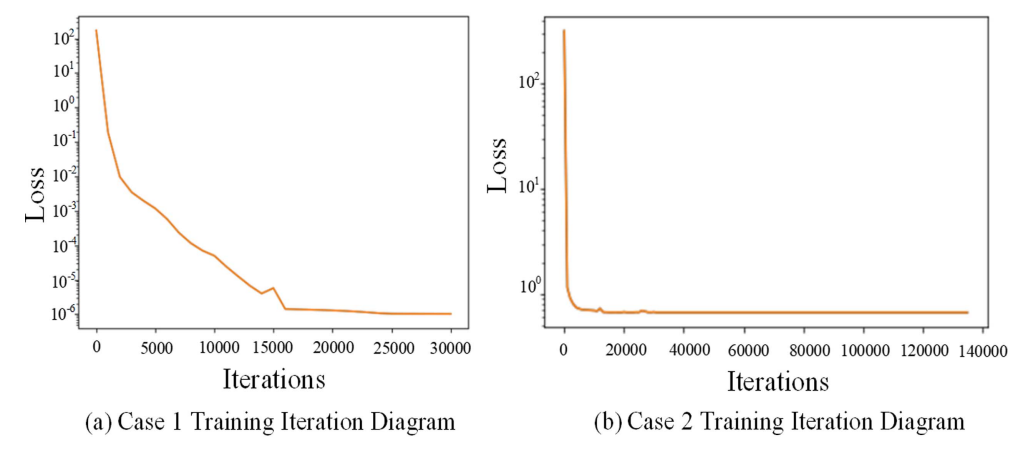


Fig. 8. (Color online) Iterative diagram for electric field case training.

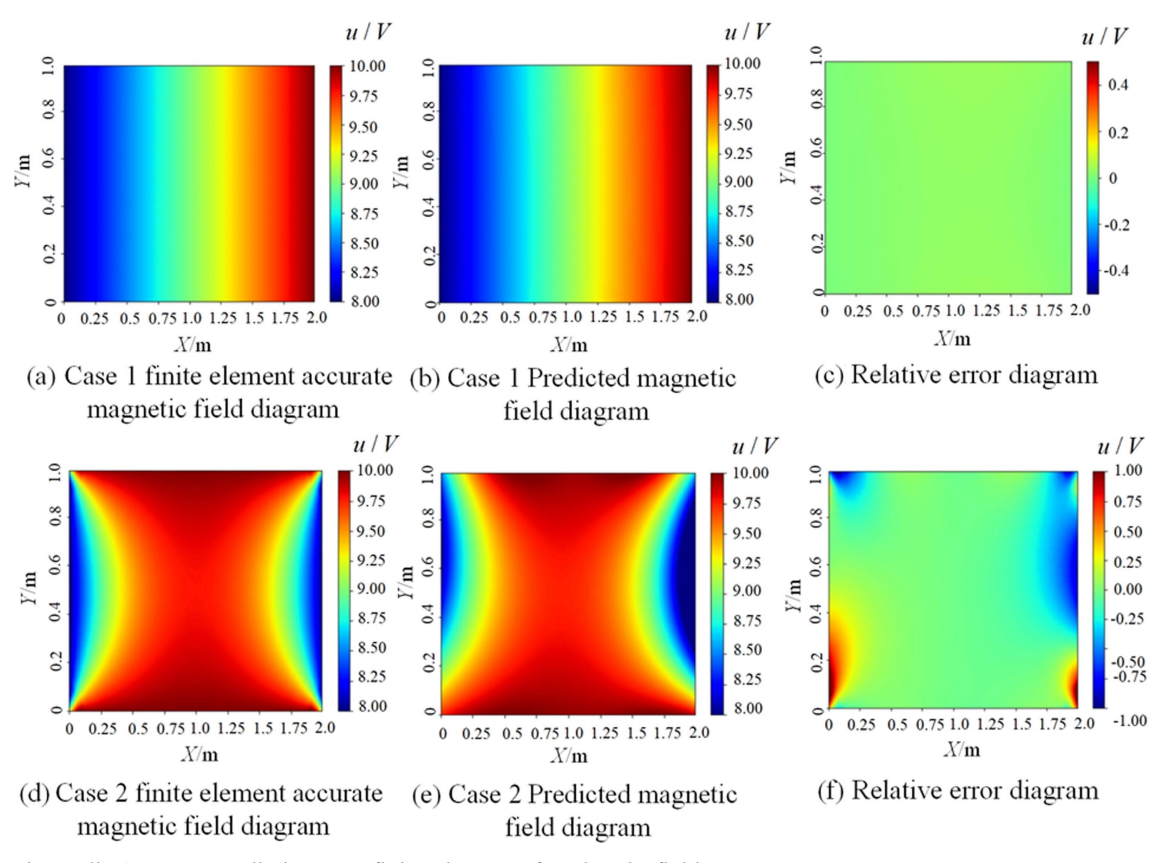


Fig. 9. (Color online) PINN predictions vs. finite elements for electric field cases.

currently, the average error percentage is determined to be 2.42%, which signifies an enhanced predictive capability and a more precise solution for the double-boundary electric field. In contrast, the four-boundary iteration map attains its minimum value within 10000 generations, yielding an average error percentage of 2.21%, thereby indicating a superior accuracy in predicting the four-boundary electric field. A comparative analysis with finite

element results demonstrates a minimal overall error, as depicted in Fig. 9 Notably, partial errors are observed only in the bottom left and bottom right corners of the four-boundary scenario, while the overall average error percentage remains comparatively low. Therefore, it can be inferred that, in the context of simple boundaries, the physical information neural network exhibits a strong correlation with finite element calculations, thereby

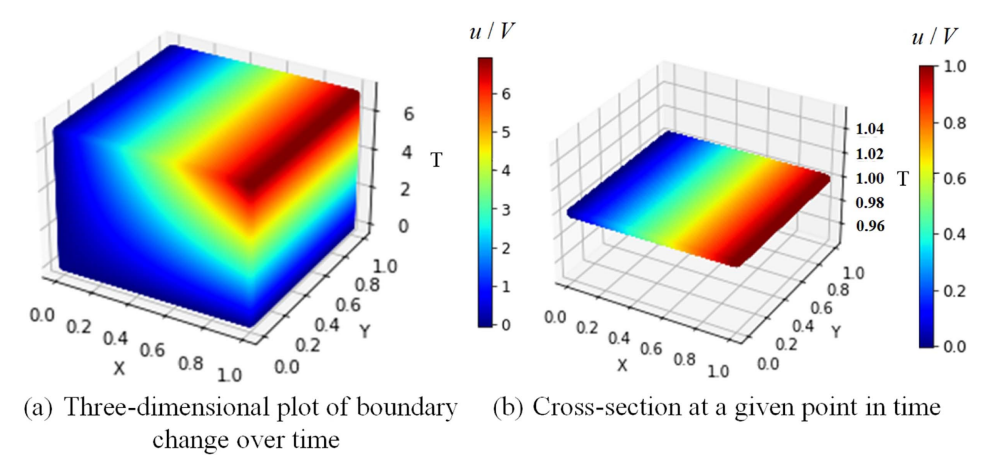


Fig. 10. (Color online) Time-varying electric field prediction map.

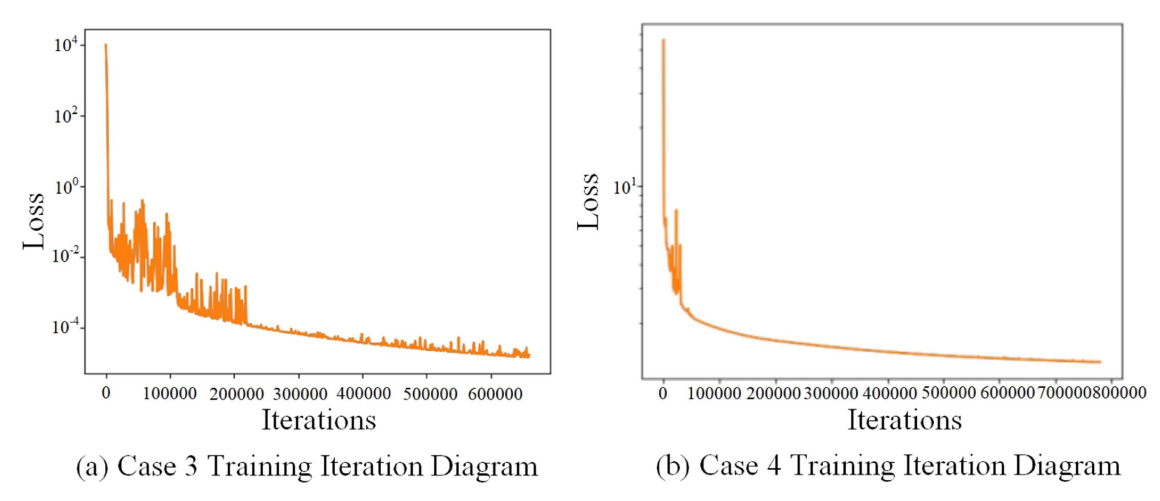


Fig. 11. (Color online) Iterative diagram for training cases with different dielectric electric fields.

delivering accurate solutions for the electric field.

The three-dimensional representation illustrated in Fig. 10 demonstrates that when the boundary is designated as T, variations along the Z-axis yield a comprehensive three-dimensional effect. Each cross-section corresponds to the solution at a specific moment, thereby enhancing overall computational efficiency and serving as a reference for temporal solutions of the electric field equation.

#### 4.2. Comparison of multi-dielectric electric field results

The analysis of the multi-media electric field training iteration diagrams presented in Fig. 11(a) and Fig. 11(b) reveals that the double-boundary iteration progressively approaches its minimum value after approximately 600000 generations, with the loss function ultimately decreasing from 10<sup>4</sup> to below 10<sup>-4</sup>. Concurrently, the average error percentage is determined to be 5.82%, indicating a satisfactory predictive capability and accurate resolution for the double-boundary electric field across various media. In contrast, the four-boundary iteration diagram demonstrates that the four-boundary iteration achieves its minimum value within 800000 generations, accompanied by an average error percentage of 3.17%, which suggests a higher accuracy in predicting the fourboundary electric field of the multi-diaphragm system. A comparative analysis with finite element results indicates a minimal overall error, as illustrated in Fig. 12. In the two-boundary scenario, the interfacial error is more pronounced, whereas in the four-boundary scenario, localized errors are observed in the upper left and upper right corners, however, the overall average error percentage remains lower. Therefore, it can be concluded that for multi-dielectric systems with simple boundaries, the outcomes generated by the physical information neural network closely correspond with finite element calculations, thereby providing precise solutions for the electric field in multi-dielectric configurations.

### 4.3. Comparison of results for multiple magnetic field quantities

The training iteration graph, specifically illustrated in Fig. 13, indicates a significant decline in the iteration count commencing around the 1000th generation, ultimately converging towards its minimum value. The loss function demonstrates a substantial reduction from an initial value of 100 to a final value of 10<sup>-5</sup>. Fig. 14 presents a comparative analysis of the predicted and actual values for four distinct magnetic field quantities. Furthermore, the average percentage of error for these quantities is calculated to be 5.54%, 5.39%, 4.06%, and 2.51%, respectively. This data suggests that the predictive model exhibits a high level of accuracy in resolving multiple magnetic field quantities. When juxtaposed with finite element methods, the overall error is observed to be lower. Consequently, it can be inferred that for simple magnetic fields, the outcomes derived from the PINN and Finite Element analyses are closely aligned, demonstrating an enhanced capability to accurately determine multiple magnetic field quantities.

# 4.4. Comparison of vector magnetic potential solutions for multi-dielectric magnetic fields in nonlinear materials

Under 50 Hz sinusoidal condition, under industrial frequency conditions, after applying an excitation voltage to the primary winding, a magnetizing current is generated to magnetize the specimen uniformly and an induced voltage is generated in the secondary winding,

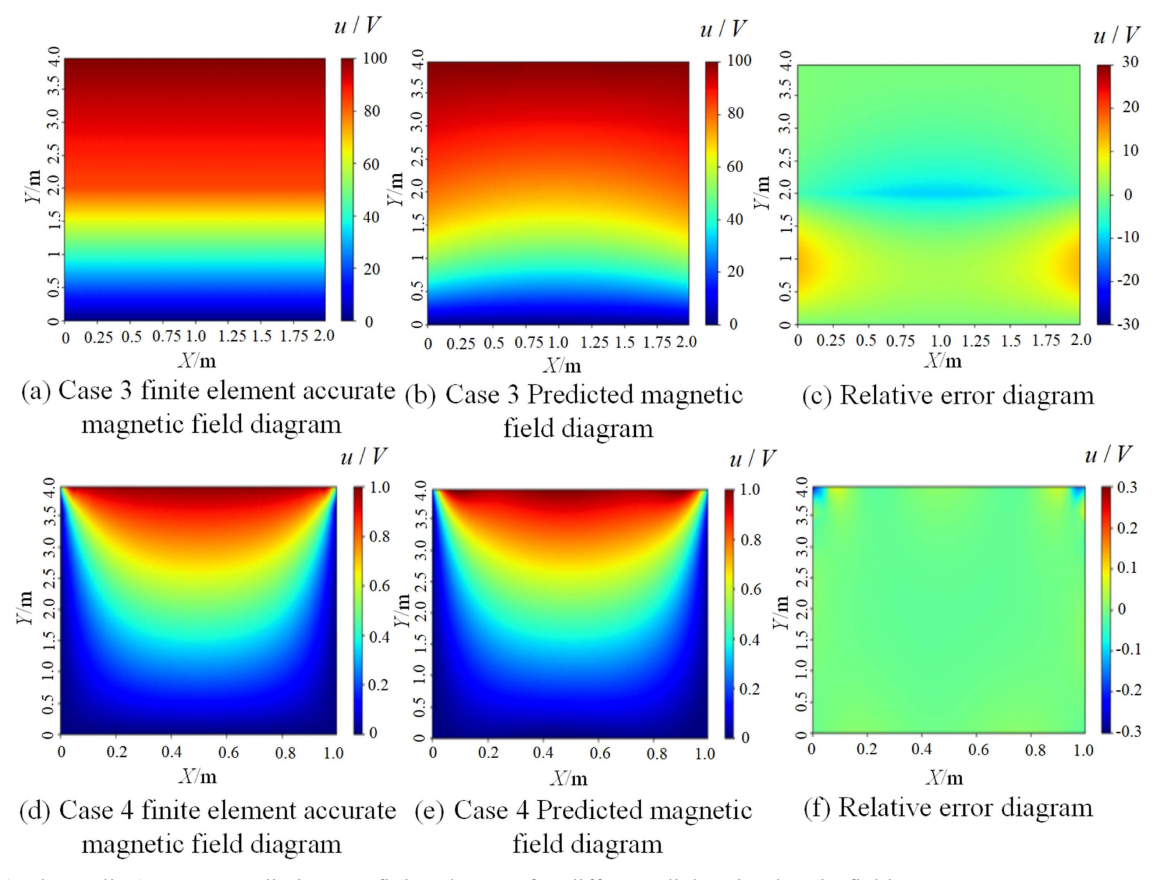


Fig. 12. (Color online) PINN prediction vs. finite element for different dielectric electric field cases.

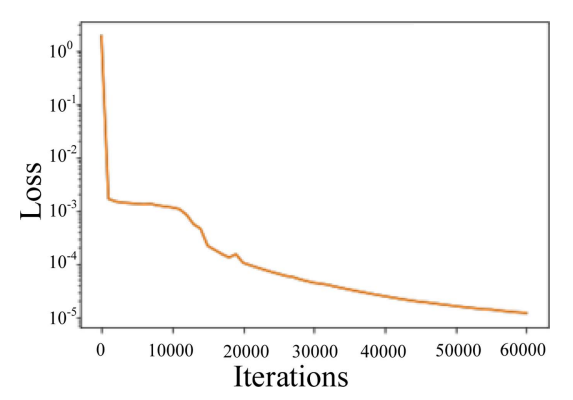


Fig. 13. (Color online) Magnetic field training iteration diagram.

and the magnetic flux density is obtained from the voltage. Fig. 15 gives the comparison between the measured and calculated values of the hysteresis return at the M-unit for the equivalent excitation voltage amplitude of  $U_{\rm max}$ =9 V and  $U_{\rm max}$ =13 V, respectively. From the figure, it can be seen that the B-H curves are in good agreement, and it can be concluded that the finite element

calculation is correct and can be further investigated.

In the context of silicon steel sheet analysis, the calculation is conducted utilizing a specific formula, wherein the number of turns is designated as 175, the current is set at 1A, and the coil area is specified as 0.0019 m². The partial differential equations are addressed through the application of PINN. Following the establishment of appropriate initial and boundary conditions, a comparative diagram of the magnetic field is generated.

The comparison illustrated in Fig. 16 indicates that the overall configuration of the magnetic vector position exhibits a notable degree of similarity, with minimal error observed. However, the presence of different media leads to a more significant error at the junction of the boundary regions. Furthermore, given the nonlinear nature of internal magnetic permeability, it is customary to employ a grid for its specification. In contrast, this study applies the PINN methodology in meshless domains, resulting in a uniform assignment of magnetic permeability for copper. This approach may introduce some inaccuracies; nonetheless, the overall predictions maintain a commendable level of accuracy.

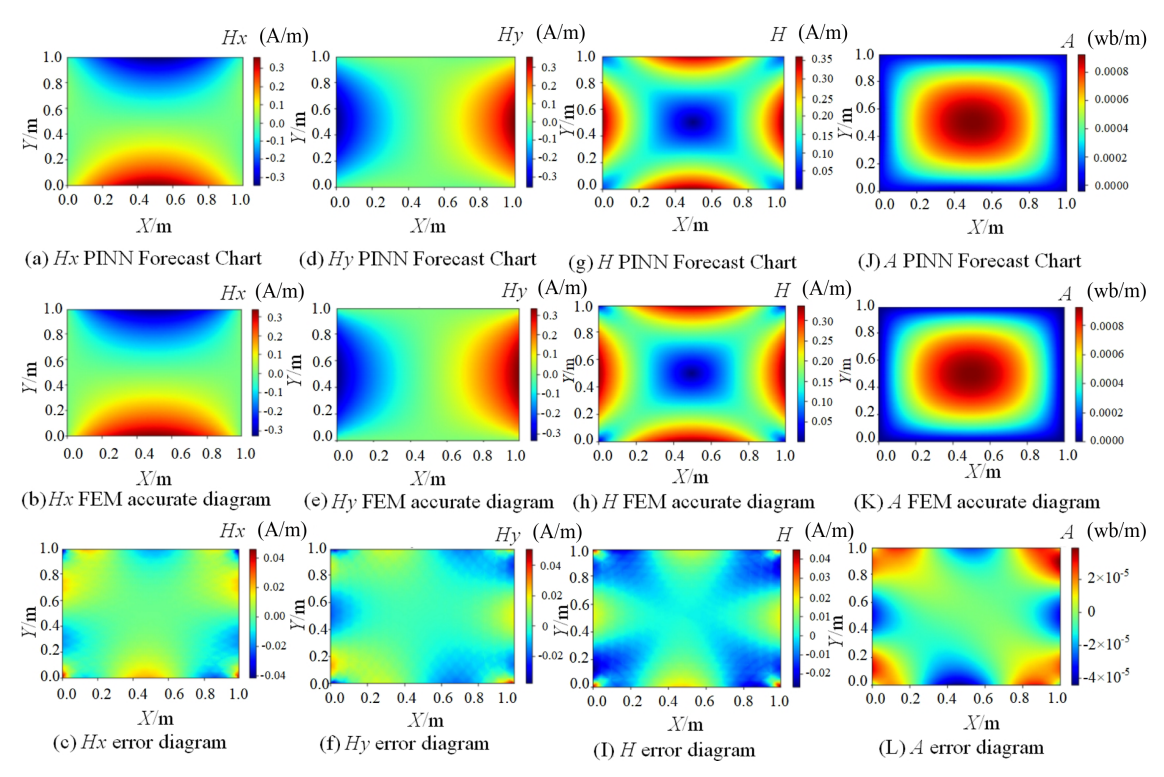


Fig. 14. (Color online) Multiple magnetic field volume predictions vs. finite elements.

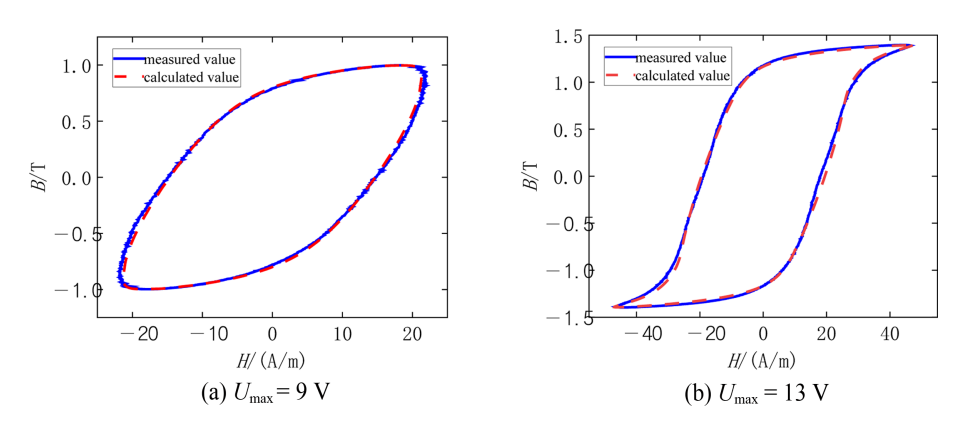


Fig. 15. (Color online) Measured vs. calculated values for voltage excitation of  $U_{\text{max}}$ =9 V and  $U_{\text{max}}$ =13 V.

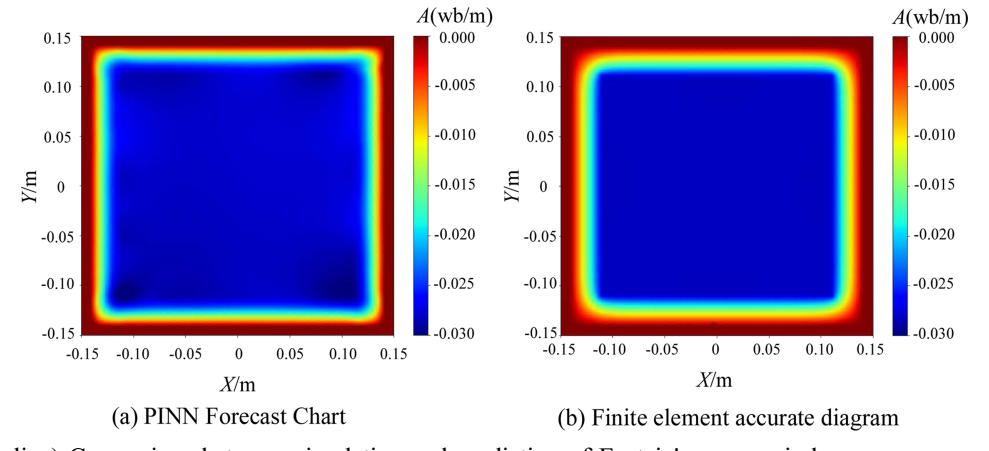
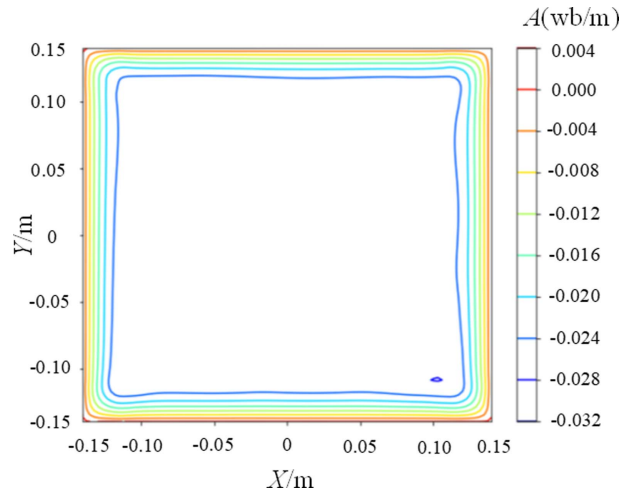


Fig. 16. (Color online) Comparison between simulation and prediction of Epstein's square circle.



**Fig. 17.** (Color online) Epstein's square circle equipotential map.

The isopotential map of the magnetic vector potential, illustrated in Fig. 17, can be derived from the predicted map. The isopotential lines exhibit a near-parallel arrangement, consistent with established theoretical principles. These isopotential lines serve as a valuable tool for investigating the underlying characteristics of the magnetic components, which is crucial for enhancing the performance prediction of electromagnetic devices through deep learning methodologies.

#### 5. Conclusion

This study proposes the application of PINN to effectively address the problem of electromagnetic field solutions, utilizing the integrated deepxde library for enhanced convenience. The findings indicate that accurate solutions can be achieved for six distinct problems without the need for labeled training data. The PINN successfully predicts the electric field distribution for simple geometries, and the solution for the electric field across various media is accomplished by differentially defining conductivity parameters pertinent to each medium. Additionally, by incorporating partial differential equations relevant to different magnetic field components, the simultaneous resolution of vector magnetic potential and magnetic field strength is facilitated, contingent upon the establishment of initial and boundary conditions. The study further explores the distribution of vector magnetic potential in nonlinear materials across multiple media, thereby improving the efficiency of magnetic field solutions. The developed framework achieves over 96% predictive fidelity for electromagnetic field distributions. Such performance enhancement directly facilitates the deployment of PINN architectures in electromagnetic engineering contexts, particularly in areas requiring precise numerical analysis and automated parameter tuning. However, the complete replacement of traditional computational methods, such as the finite element method, with PINN is currently impractical due to the extensive training time required. Nonetheless, the integration of PINN with conventional solvers presents a promising avenue for future research. By leveraging the proposed PINN framework, researchers can explore sophisticated network architectures and techniques, including attention-based neural networks (such as transformers), to further enhance the performance of PINNs.

#### Acknowledgment

This work was supported by the National Natural Science Foundation of China under Grant No. 52477011, 52207012.

#### References

- L. Kielhorn, T. Rüberg, and J. Zechner, COMPEL 36, 1540 (2017).
- [2] A. Demenko and J. Sykulski, COMPEL 33, 47 (2013).
- [3] L. Jin, Y. Liu, Q. Yang, C. Zhang, and S. Liu, COMPEL **42**, 90 (2023).
- [4] A. Géron, Hands-On Machine Learning with Scikit-Learn, Keras, and TensorFlow, 2nd Edition, O'Reilly Media, Inc, Newton (2019) pp. 111-200.
- [5] W. Tang, T. Shan, X. Dang, M. Li, F. Yang, and S. Xu, and J. Wu, IEEE Electrical Design of Advanced Packaging and Systems Symposium (EDAPS) (2017) pp. 1-3.
- [6] S. Barmada, N. Fontana, L. Sani, D. Thomopulos, and M. Tucci, IEEE Trans. Magn. 56, 7513604 (2020).
- [7] R. Gong and Z. Tang, COMPEL 39, 959 (2020).
- [8] A. Khan, V. Ghorbanian, and D. Lowther, IEEE Trans Magn. 55, 7202304 (2019).
- [9] M. M. Rahman, A. Khan, D. Lowther, and D. Giannacopoulos, COMPEL 42, 1115 (2023).
- [10] A. Belkallouche, T. Rezoug, L. Dala, and K. Tan, Aircr. Eng. Aerosp. Technol. 94, 1422 (2022).
- [11] M. Ghalambaz, M. A. Sheremet, M. A. Khan, Z. Raizah, and J. Shafi, Int. J. Numer. Methods Heat & Fluid Flow **34**, 3131 (2024).
- [12] G. Z. Zeng, Z. W. Chen, Y. Q. Ni, and E. Z. Rui, Int. J. Numer. Methods Heat & Fluid Flow 34, 2963 (2024).
- [13] G. Zhou, M. Zhan, D. Huang, X. Lyu, and K. Yan, Ind. Lubric. Tribol. 76, 1246 (2024).
- [14] B. Huang and J. Wang, IEEE Trans. Power. Syst. **38**, 572 (2023).
- [15] A. Yazdani, L. Lu, M. Raissi, and G. E. Karniadakis, PLoS Comput. Biol. 16, e1007575 (2020).

- [16] Q. Lou, X. Meng, and G. E. Karniadakis, J. Comput. Phys. **447**, 110676 (2021).
- [17] A. Saba, C. Gigli, A. B. Ayoub, and D. Psaltis, Adv. Photon. 4, 066001 (2022).
- [18] K. Shukla, A. D. Jagtap, J. L. Blackshire, D. Sparkman, and G. E. Karniadakis, IEEE Signal. Process. Mag. 39, 68 (2022).
- [19] C. M. Jiang, S. Esmaeilzadeh, K. Azizzadenesheli, K. Kashinath, M. Mustafa, H. A. Tchelepi, P. Marcus, M. Prabhat, and A. Anandkumar, SC '20: Proceedings of the International Conference for High Performance Computing, Networking, Storage and Analysis (SC20), online (2020) pp. 1-15.
- [20] X. Aguilar and S. Markidis, IEEE International Conference on Cluster Computing (CLUSTER) IEEE (2021) pp. 692-697.

- [21] A. Beltrán-Pulido, I. Bilionis, and D. Aliprantis, IEEE Trans. Energy. Convers. **37**, 2678 (2022).
- [22] A. Kovacs, L. Exl, A. Kornell, J. Fischbacher, M. Hovorka, M. Gusenbauer, L. Breth, H. Oezelt, D. Praetorius, D. Suess, and T. Schrefl, J. Magn. Magn. Mater. 548, 168951 (2022).
- [23] S. Markidis, Front. Big. Data. 4, 669097 (2021).
- [24] L. Lu, R. Pestourie, W. Yao, Z. Wang, F. Verdugo, and S. G. Johnson, SIAM J. Sci. Comput. 43, B1105 (2021).
- [25] A. Khan and D. A. Lowther, IEEE Trans. Magn. 58, 7500404 (2022).
- [26] Z. Gong, Y. Chu, and S. Yang, IEEE Trans. Magn. **59**, 7002005 (2023).
- [27] L. Lu, X. Meng, Z. Mao, and G. E. Karniadakis, SIAM Review **63**, 208 (2021).